Supporting Information

Marrying V_5S_8 and Sb_2S_3 for volume-tolerant and high-rate potassium-ion storage

Yulian Dong,[a,b] Yubin Fu,[c,d] Vincent Hartmann,[b] Changfan Xu,[b] Ping Hong,[b] Yueliang Li,[e] Huaping Zhao,[b] Weidong Shi,*[a] Ute Kaiser,*[e] and Yong Lei*[b]

[a]College of Environmental and Chemical Engineering, Jiangsu University of Science and Technology, Zhenjiang 212003, China
Email: swd1978@ujs.edu.cn

[b]Fachgebiet Angewandte Nanophysik, Institut für Physik & IMN MacroNano, Technische Universität Ilmenau, 98693 Ilmenau, Germany
Email: yong.lei@tu-ilmenau.de

[c]School of Energy and Environment, Southeast University, Nanjing, 211189 Jiangsu, China

[d]Center for Advancing Electronics Dresden (cfaed) & Faculty of Chemistry and Food Chemistry, Technische Universität Dresden, 01062 Dresden, Germany

[e]Central Facility for Electron Microscopy, Electron Microscopy Group of Materials Science, Ulm University, Ulm, 89081, Germany
Email: ute.kaiser@uni-ulm.de

Theoretical Calculation. Version 6.3.1 of the Vienna Ab initio Simulation Package (VASP) has been utilized to DFT-based first-principles computations.[1,2] The electronic states were represented by a plane-wave basis set with a kinetic energy cutoff fixed at 520 eV. The interaction between core and valence electrons was modeled through the projector augmented wave (PAW) method.[3] The exchange-correlation functional was approximated by the Perdew–Burke–Ernzerhof (PBE) generalized gradient approximation (GGA)[4,5] To properly account for the electron correlations in the V 3d orbitals, a DFT+U correction was applied, with on-site Coulomb and exchange parameters (U = 3 eV & J = 1 eV).

Surface models were constructed using a 2×1 supercell for the Sb_2S_3(101) plane and a 1×1 supercell for the V_5S_8(220) facet. Decoupling between periodic images was achieved with a 15 Å vacuum layer perpendicular to the slab. During geometry optimization, all atoms, including Sb, V, and O, until residual forces were below 0.02 eV/Å. K-point testing of the Brillouin zone was conducted utilising Monkhorst-Pack grids: 2×2×1 for surface structures and 6×4×2 for density of states (DOS) evaluations.[6] Pre-and post-processing of VASP output files was conducted using the VASPKIT software package.[7]

The diffusion barriers for potassium (K) atoms on the material surfaces were computed along the lowest energy migration pathways adopting the climbing image nudged elastic band (CI-NEB) method, executed with the VTST tools in VASP. The Fermi level offset across materials was calculated using the average electrostatic potential V for interface energy alignment analysis. Using this method, interface Fermi level alignment may be assessed:

$$\Delta E_{F}^{V5S8/Sb2S3} = \left(E_{F}^{Sb2S3} - V^{Sb2S3}\right) - \left(E_{F}^{V5S8} - V^{V5S8}\right) - \Delta V^{V5S8/Sb2S3}$$

Characterizations. The crystal structures of ultrathin nanoribbon structures, were analyzed using X-ray diffraction (XRD) with a SIEMENS D5000 diffractometer. Samples were taken over a 2θ range of 10°-70°, working with Cu Kα radiation generated from a copper anode. Surface chemical compositions and oxidation states were probed via X-ray photoelectron spectroscopy (XPS), utilizing a Thermo Scientific K-Alpha detector. To investigate vibrational properties, Raman spectroscopy was conducted using an NT-MDT equipment (532 nm laser), targeting characteristic D and G bands along with vibrational features of metal–sulfur bonds. SEM (Hitachi S-4800)

as well as HRTEM (JEOL JEM-2100F) observed material surface morphology and internal crystal structure. The synthesized materials' thermal stability was assessed by thermogravimetric (TG) measurement in nitrogen. The Netzsch TG 209 F1 Iris thermal analyzer was used to measure samples at 30–1000 °C in aluminum crucibles at a constant heating rate of 10 °C/min.

Electrochemical Measurements. The active material was blended with Super P conductive carbon and CMC binder in a weight ratio of 7:2:1 to make three active materials electrodes. The resulting homogeneous slurry was applied onto Cu foil, ensuring mass loading between 1-2 mg/cm^2. Subsequently, a vacuum oven at 105 °C was used for 12 hours of drying. In an argon-filled glovebox with both water and oxygen condensate ≤ 0.1 ppm, CR2032-type coin cells were built for electrochemical testing. A glass microfiber membrane separated the anode and counter electrodes, where a potassium metal disc was used. For contamination prevention, the electrolyte solution (5 M KFSI) was dissolved in 1,2-dimethoxyethane (DME) in an inert nitrogen environment. A Land CT 2001A battery equiment (Land, China) was used to galvanostatic cycles and GITT at ambient temperature. A VSP electrochemical workstation (Bio-Logic, France) was used for further electrochemical characterizations, including electrochemical impedance spectroscopy (EIS) as well as cyclic voltammetry (CV).

Potassium deposition behavior of V_5S_8/Sb_2S_3@NC at 500× (Video S1)

The investigation of potassiation-induced morphological alterations behavior on the target electrode was conducted utilizing Nikon optical microscopes.

Supporting Figures and Tables

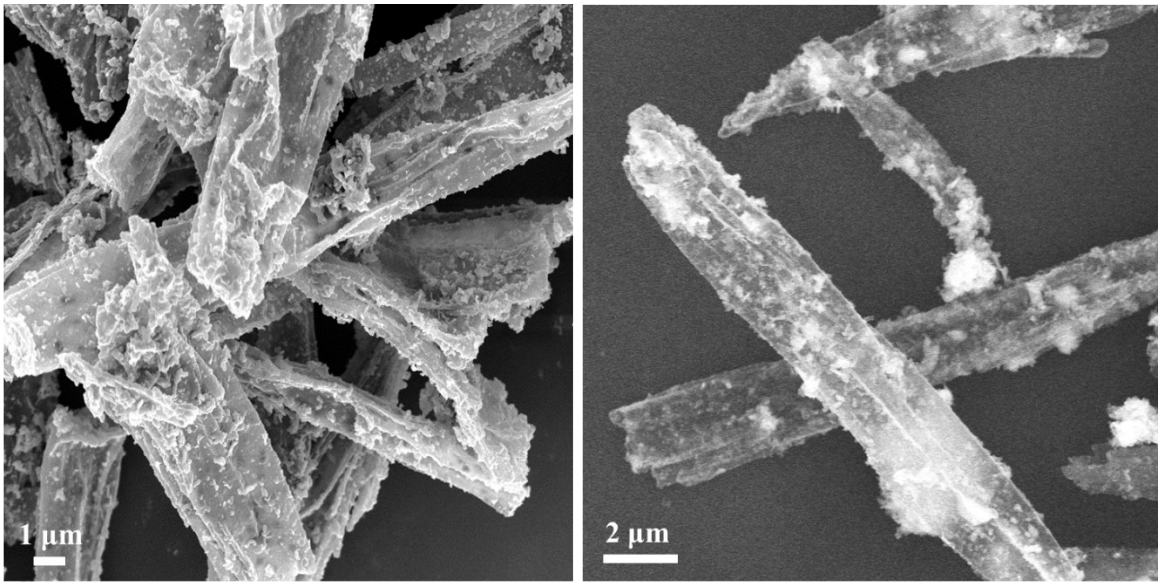

Fig. S1 SEM images of the molar ratio of precursor vanadium source and antimony source =1:1.

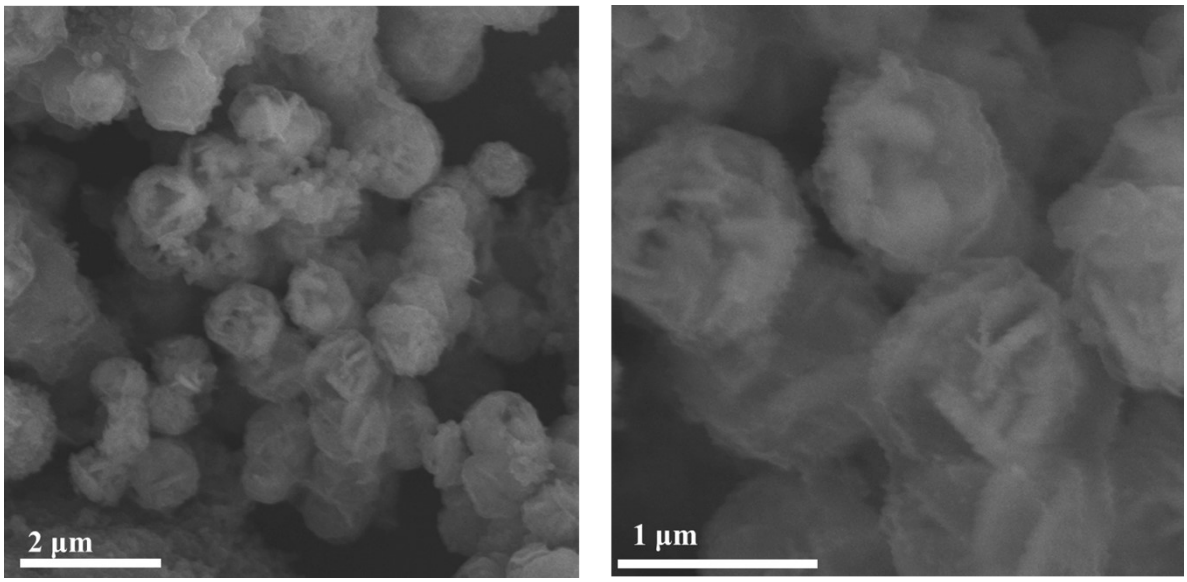

Fig. S2 SEM images of V_5S_8@NC nanoflower.

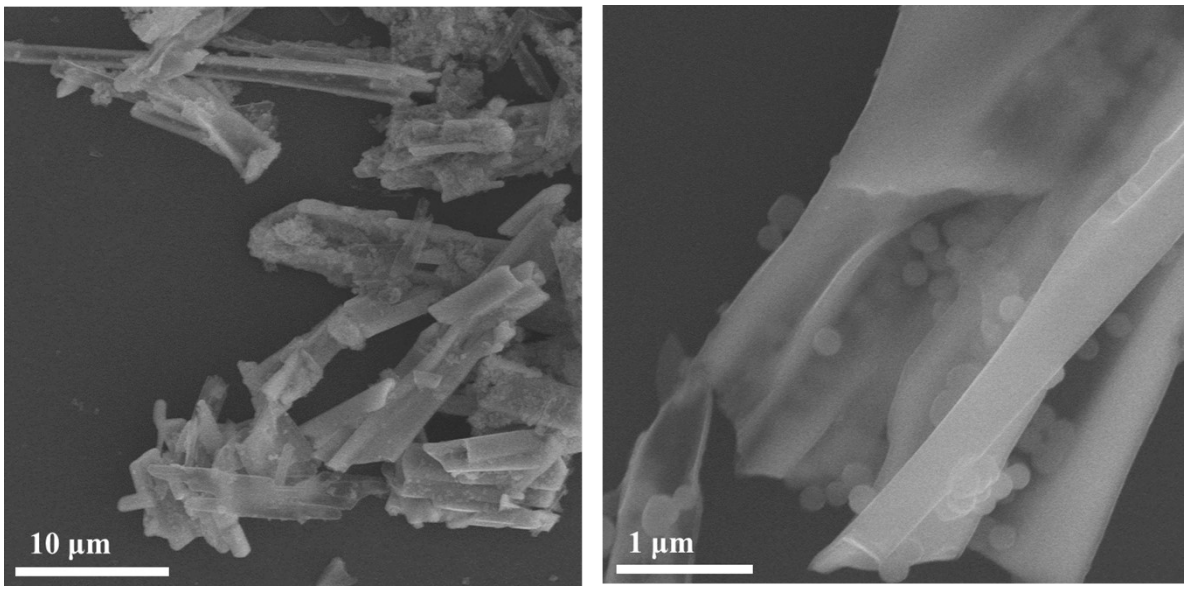

Fig. S3 SEM images of Sb_2S_3@NC nanorod.

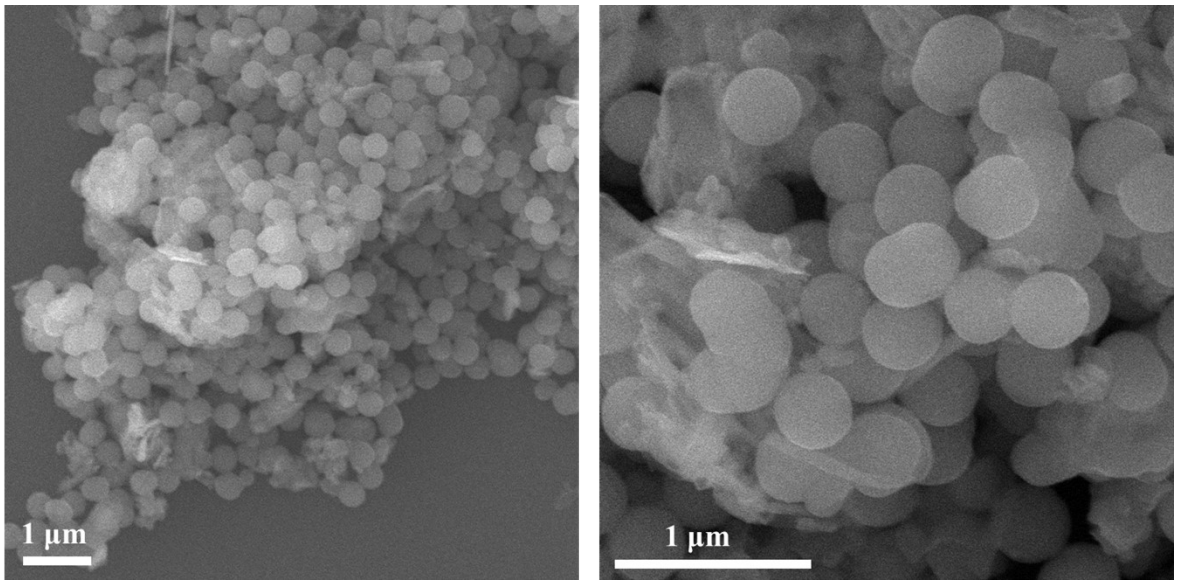

Fig. S4 SEM images of the molar ratio of precursor vanadium source and antimony source =3:1.

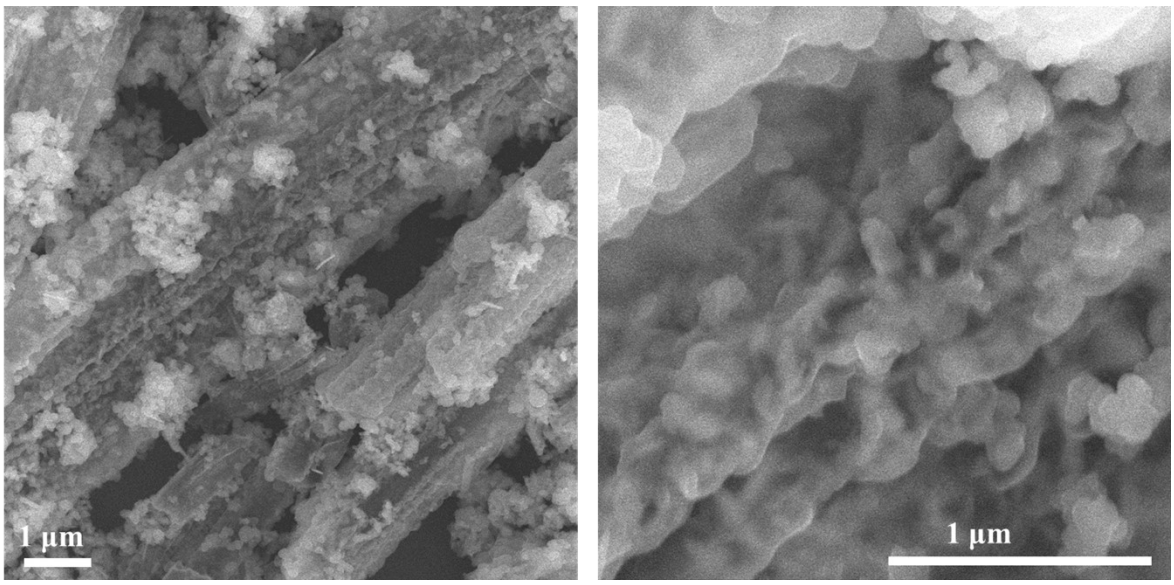

Fig. S5 SEM images of the molar ratio of precursor vanadium source and antimony source =1:3.

The morphology of the V_5S_8/Sb_2S_3@NC heterostructure can be effectively tuned by varying the molar ratio of the precursor vanadium and antimony sources (Fig. S1, S4, and S5). At a 1:1 ratio, well-defined nanoribbon structures with uniformly distributed V_5S_8 are obtained, whereas deviation from this ratio leads to particle aggregation or non-uniform phase distribution. This morphology evolution is likely associated with the difference in nucleation and growth behavior under different precursor ratios, as commonly observed in sulfide systems.

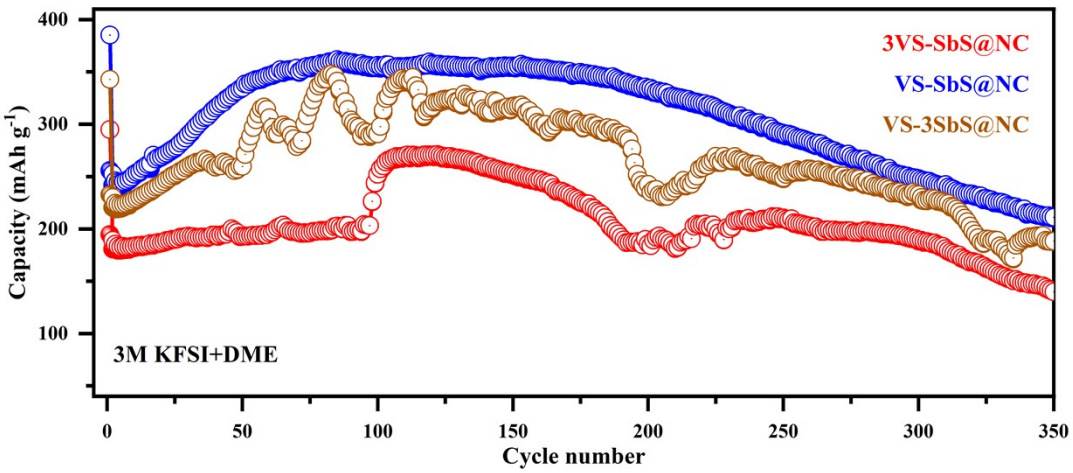

Fig. S6 Long–term cycling performance of the of the molar ratio of precursor vanadium source and antimony source electrodes at a current density of 1 A g^{-1} with 3M KFSI in DME.

As shown in Fig. S6, the electrochemical performance of the composites is strongly dependent on the precursor molar ratio. The sample prepared at a ratio of 1:1 delivers the highest reversible capacity and the best cycling stability among the three compositions. In contrast, the V-rich sample (3:1) exhibits lower capacity and faster capacity decay, while the Sb-rich sample (1:3) shows intermediate performance. Combined with the morphological analysis, these results suggest that the optimized nanoribbon structure and more uniform phase distribution at the 1:1 ratio is beneficial for maintaining structural integrity and facilitating ion transport during cycling. Therefore, the precursor ratio of 1:1 was selected for subsequent studies.

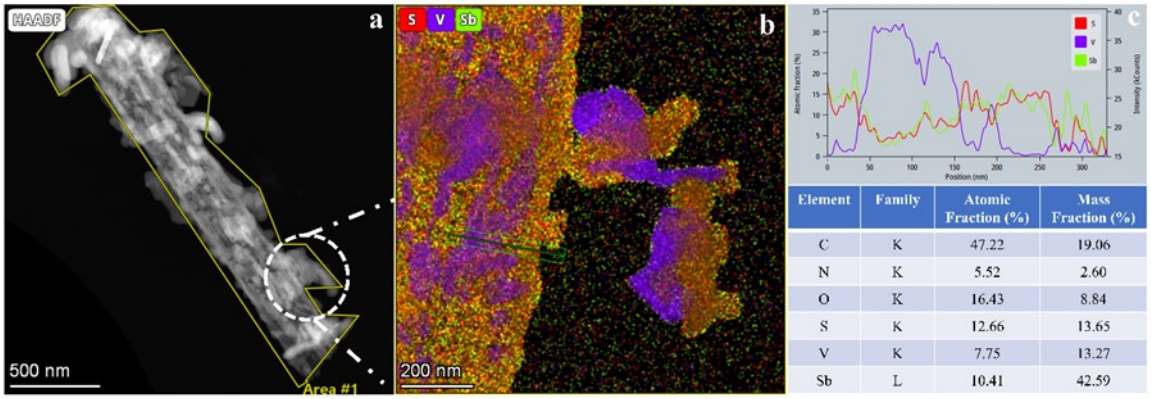

Element	Family	Atomic Fraction (%)	Mass Fraction (%)
C	K	47.22	19.06
N	K	5.52	2.60
O	K	16.43	8.84
S	K	12.66	13.65
V	K	7.75	13.27
Sb	L	10.41	42.59

Fig. S7 HAADF-STEM image(a), EDS elemental mapping of S, V, Sb (b), line-scan profiles and corresponding quantitative analysis (c) of the V_5S_8:Sb_2S_3@NC heterostructure.

The results show that V is mainly distributed on the surface of Sb_2S_3 nanoribbons. The local V_5S_8:Sb_2S_3 ratio is estimated to be in the range of ~0.30–0.40:1, as shown in Fig. S7. Considering the local nature of EDS and the carbon support, this result is semi-quantitative, indicating an Sb_2S_3-dominant structure with surface-dispersed V_5S_8.

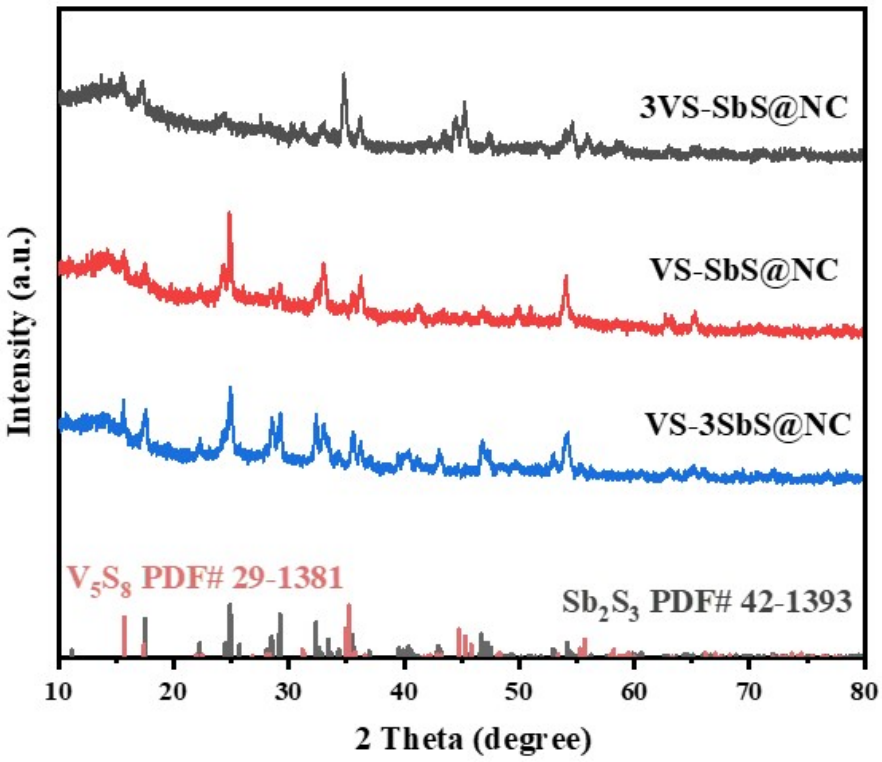

Fig. S8 XRD profiles of the molar ratio of precursor vanadium source and antimony source.

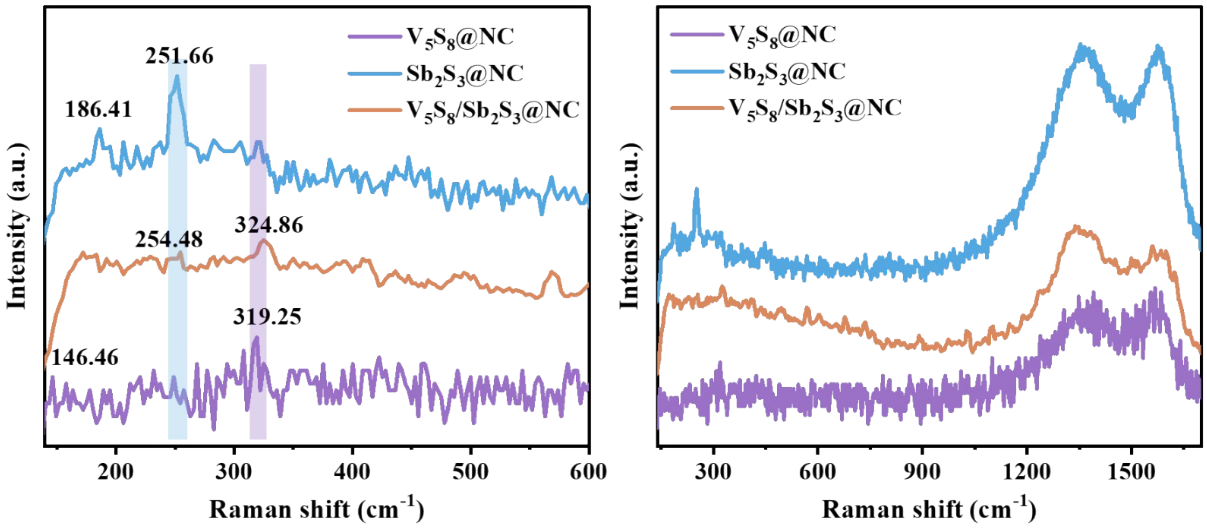

Fig. S9 Raman profiles of V_5S_8/Sb_2S_3@NC, V_5S_8@NC, and Sb_2S_3@NC.

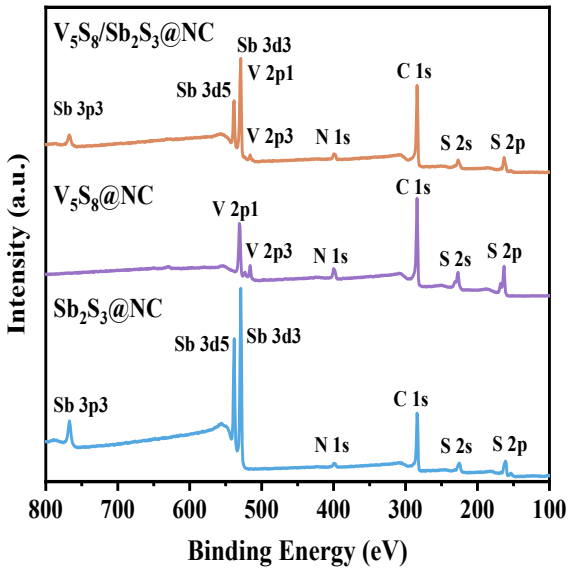

Fig. S10 XPS survey spectrum of V_5S_8/Sb_2S_3@NC, V_5S_8@NC, and Sb_2S_3@NC.

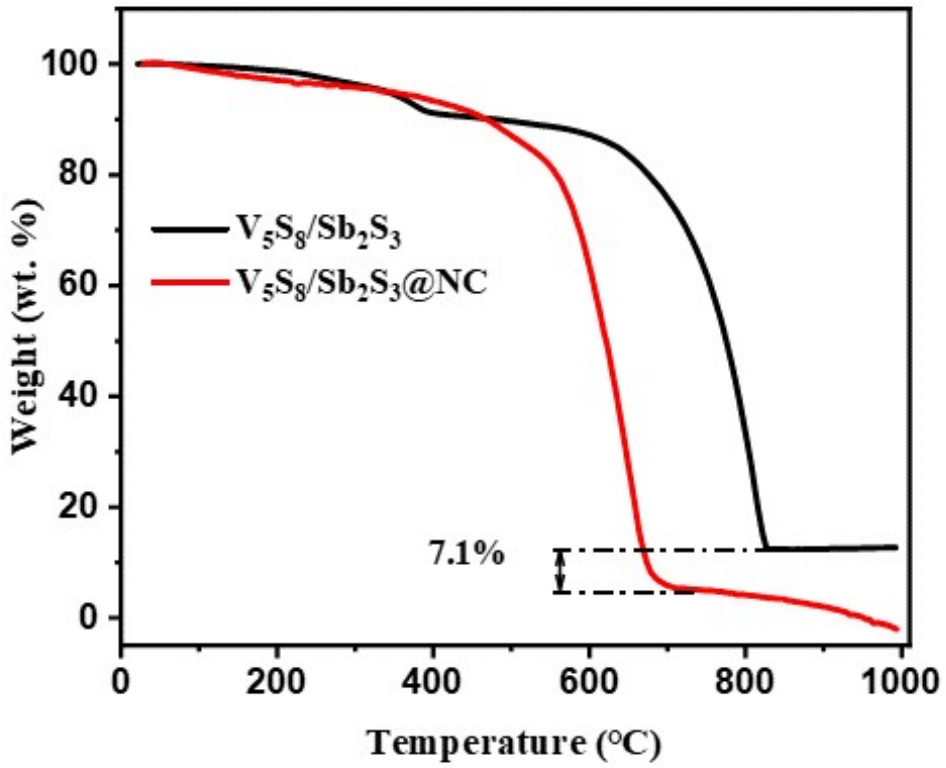

Fig. S11 Thermogravimetric analyzer curves of V_5S_8/Sb_2S_3 and V_5S_8/Sb_2S_3@NC at a constant heating rate 10℃/min under a nitrogen atmosphere.

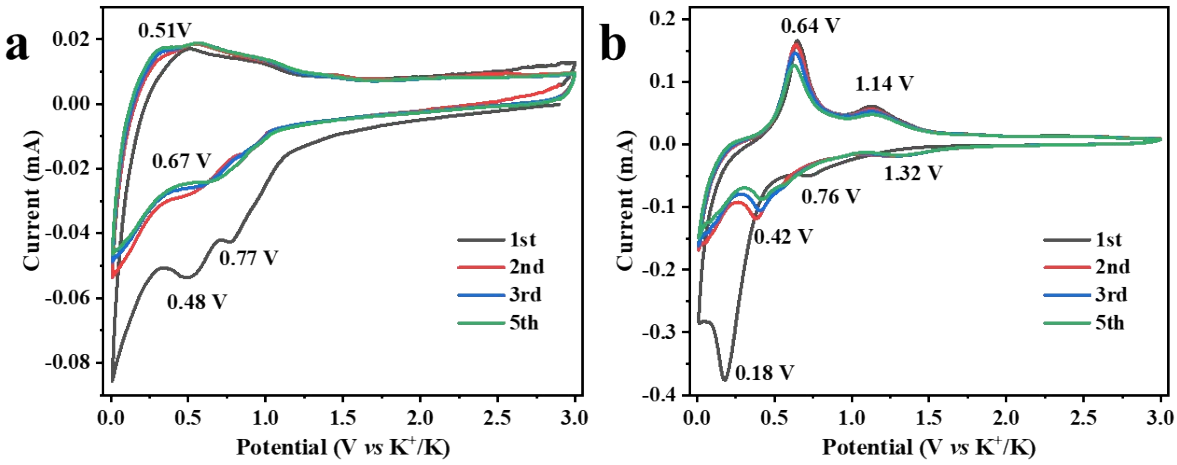

Fig. S12 Cyclic voltammograms at a scan rate of 0.1 mV s^{-1} of a) V_5S_8@NC and b) Sb_2S_3@NCelectrodes.

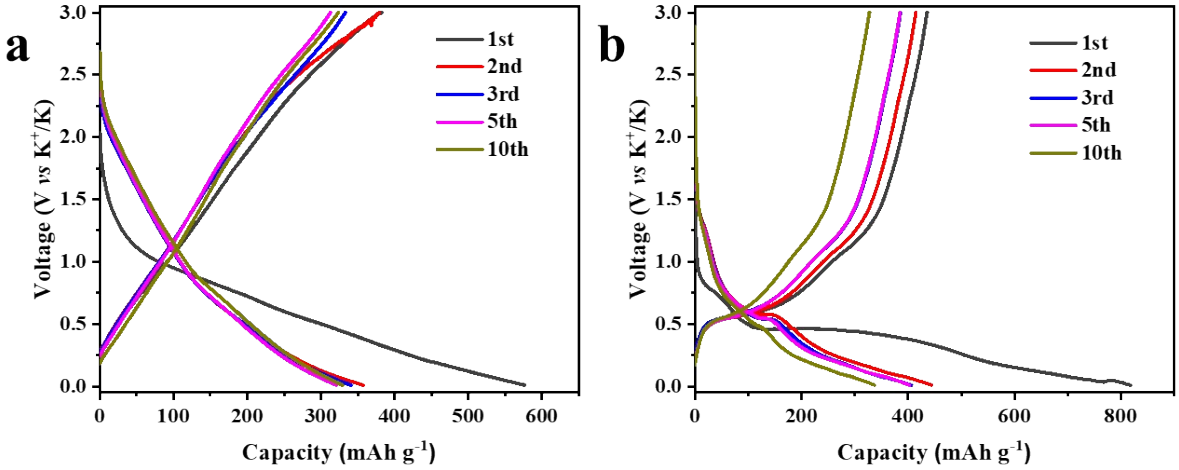

Fig. S13 Cyclic voltammograms at a current density of 0.1 A g^{-1} of a) V_5S_8@NC and b) Sb_2S_3@NC electrodes.

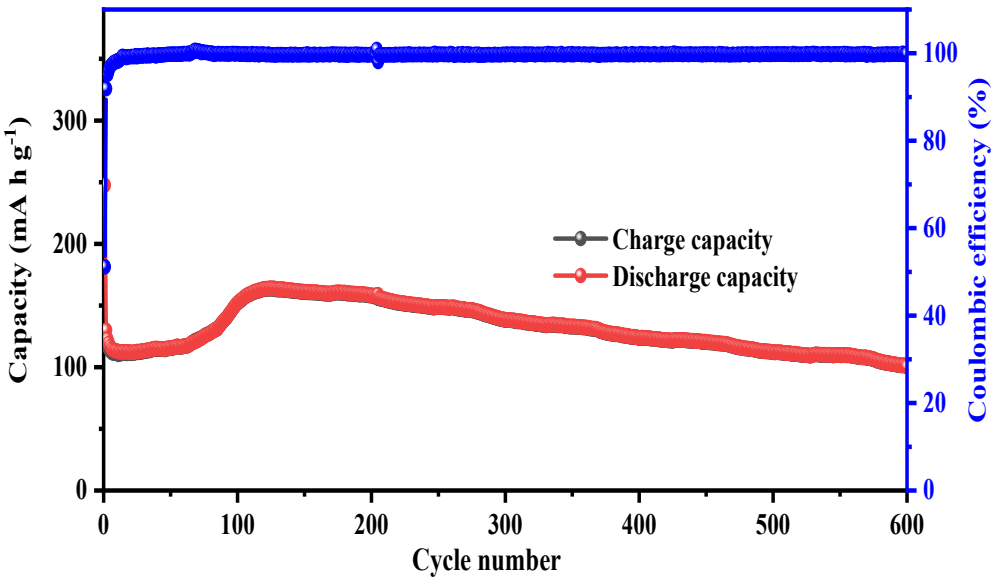

Fig. S14 Long–term cycling performance of the V_5S_8@NC electrodes at a current density of 1 A g^{-1}.

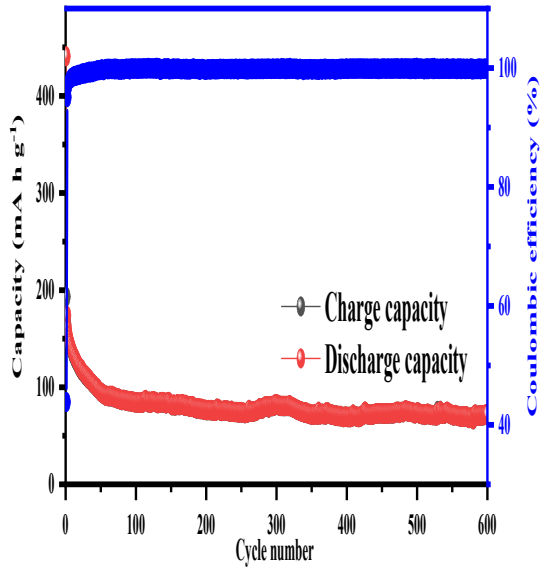

Fig. S15 Long–term cycling performance of the Sb_2S_3@NC electrodes at a current density of 1 A g^{-1}.

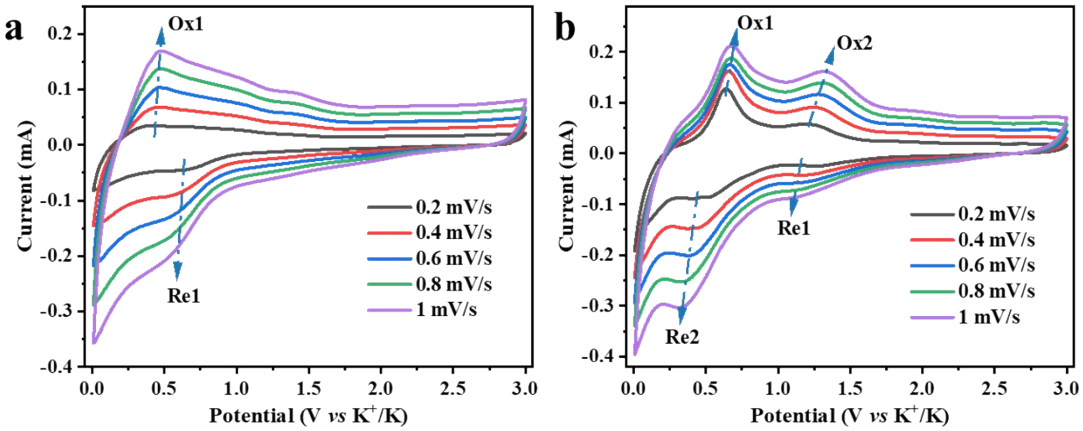

Fig. S16 CV curves at various sweep rates of a) V_5S_8@NC and b) Sb_2S_3@NC electrodes.

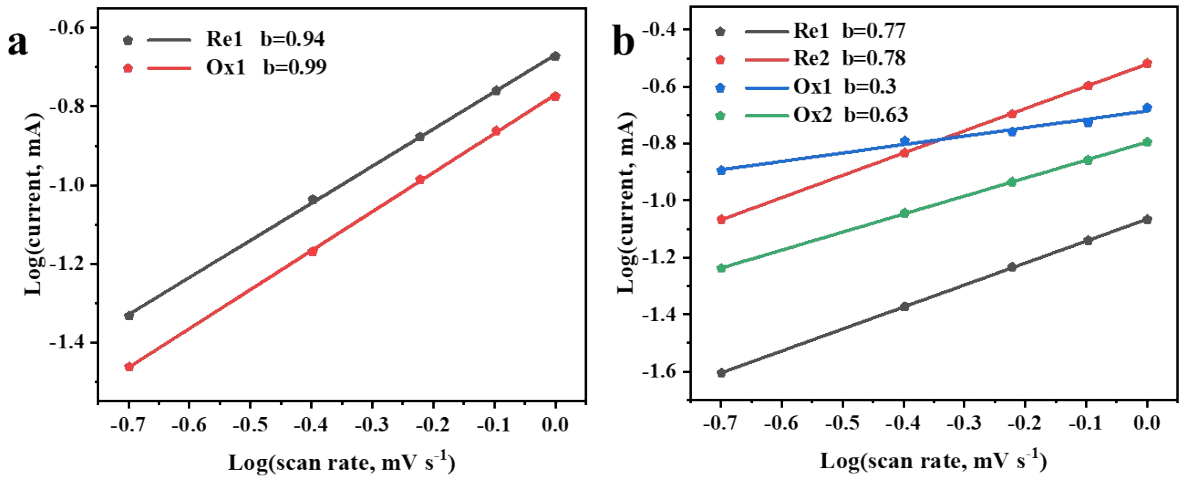

Fig. S17 Logarithmic linear relationship between peak current and sweep rates of a) V_5S_8@NC, b) Sb_2S_3@NC electrodes.

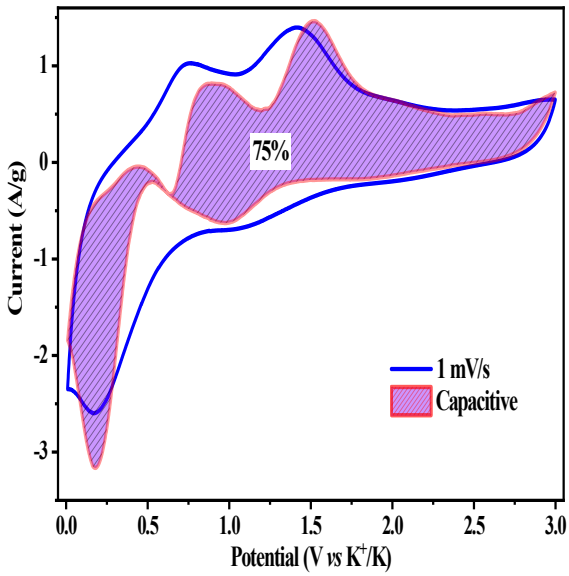

Fig. S18 CV curves of V_5S_8/Sb_2S_3@NC, separation of total current (blue line) and surface capacitive current (purple area) at 1 mV s^{-1}.

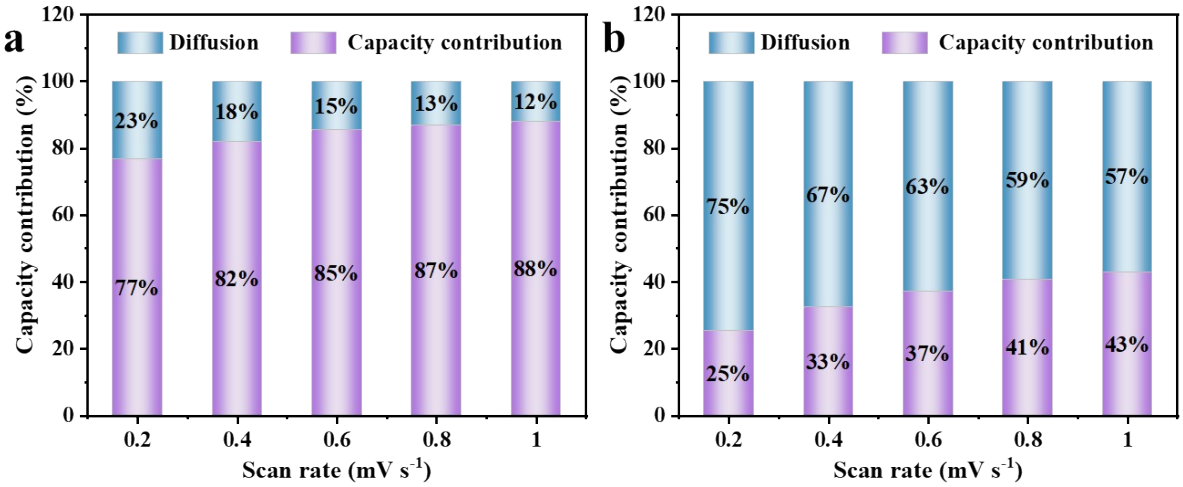

Fig. S19 Capacity ratios between diffusion and capacitive contribution of a) V_5S_8@NC, b) Sb_2S_3@NC electrodes.

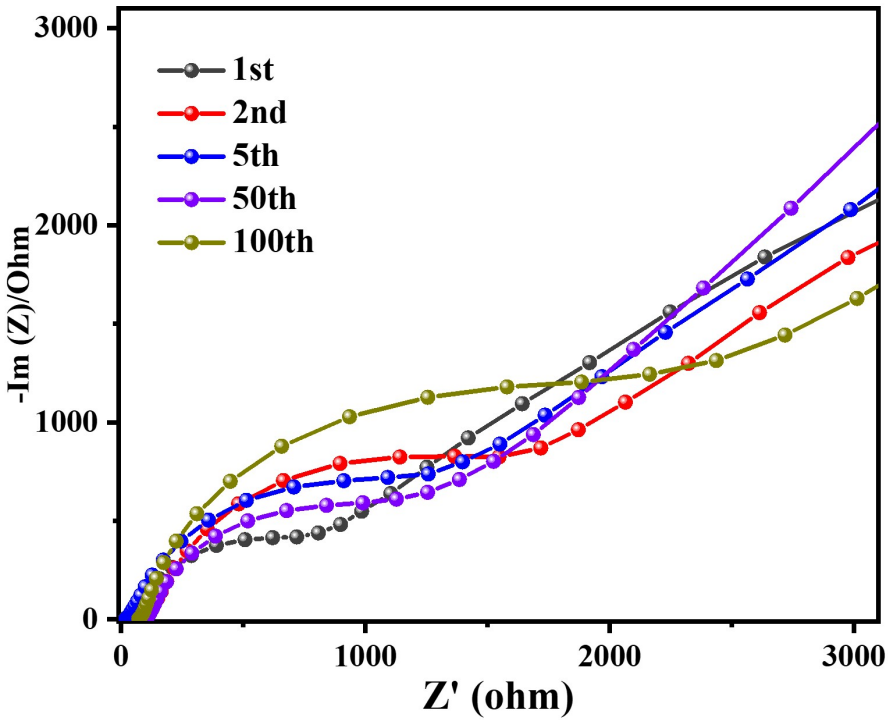

Fig. S20 EIS of V_5S_8/Sb_2S_3@NC electrode at different cycles.

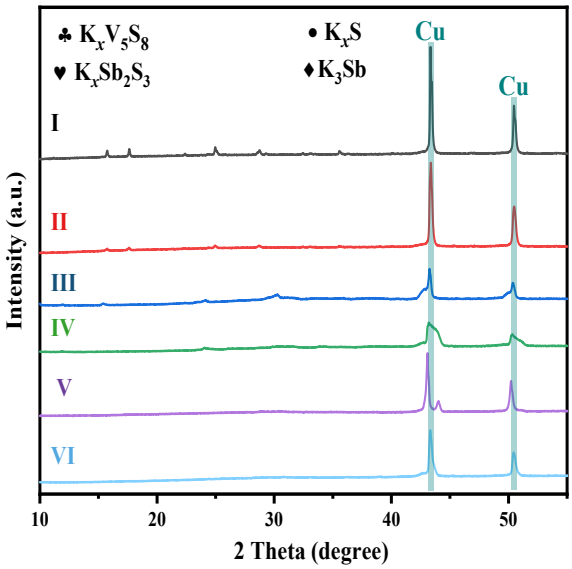

Fig. S21 Ex–situ XRD patterns at various potential states in the first cycle.

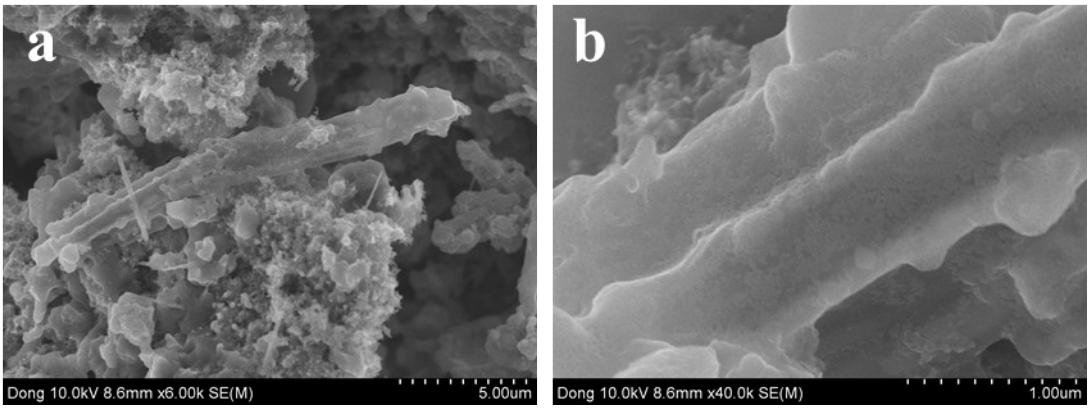

Fig. S22 SEM images of the V_5S_8/Sb_2S_3@NC electrodes after first cycle.

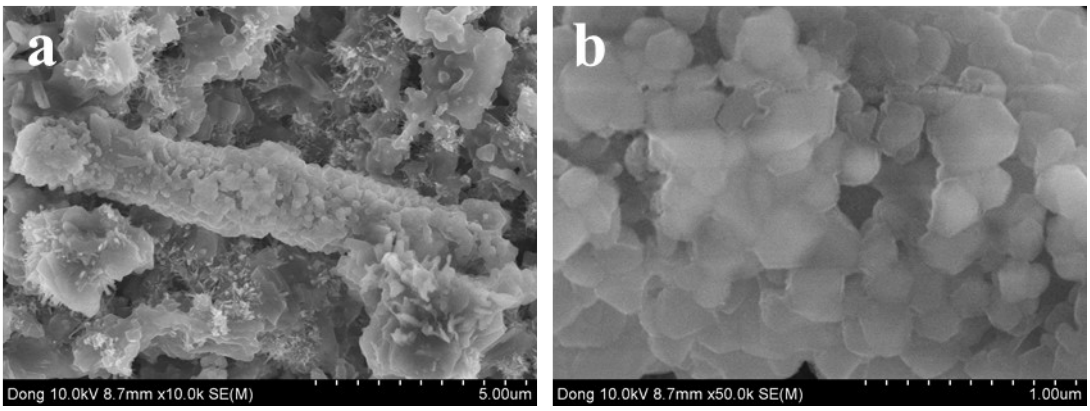

Fig. S23 SEM images of the V_5S_8/Sb_2S_3@NC electrodes after 100th cycle.

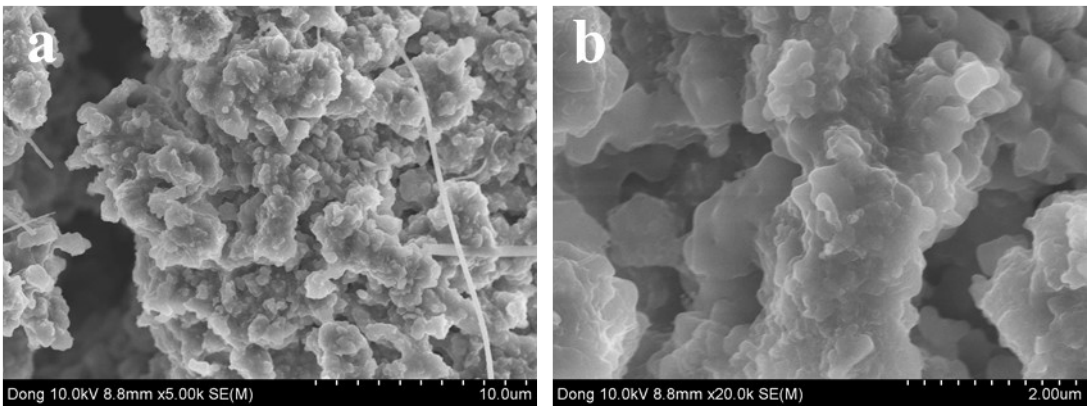

Fig. S24 SEM images of the V_5S_8/Sb_2S_3@NC electrodes 700th cycle.

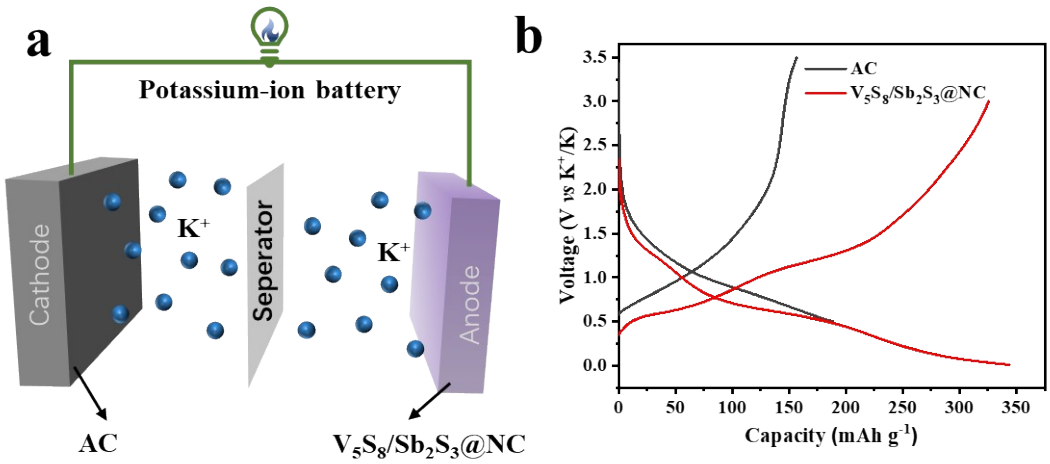

Fig. S25 Electrochemical performance of the PIB full battery: (a) Schematic illustration of the PIB full battery, (b) discharge–charge profiles of AC cathode and V_5S_8/Sb_2S_3@NC anode.

Fig. S26 Cycling stability of the full battery at a current density of 0.1 A g^{-1}.

Table S1. Comparison of potassium ion storage performance of V_5S_8/Sb_2S_3@NC and transition–metal sulfides composites.

No	Anode materials	Voltage window (V *vs*. K^+/K)	Electrolyte	Capacity mA h g^{-1} /Cycles / Current density A g^{-1}	Cycling stability (Capacity mA h g^{-1} / Cycles / Current density A g^{-1})	Ref.
	V_5S_8/Sb_2S_3@NC	0.01–3	5M KFSI/DME	484.7 / 100 / 0.1	301.5 / 600 / 1	This work
		0.01-3	3M KFSI/DME		229.1 / 350 / 1	This work
1	V_3S_4@C	0.01–3	–	432 / 100 / 0.05	182 / 4000 / 1	[8]
2	D–V_5S_8/CNFs	0.01–3	1M KFSI/DME	350 / 70 / 0.1	165 / 3000 / 1	[9]
3	SnS_2-Cu/GO@PDA	0.01–3	1M KFSI/EC+DEC	391.8 / 100 / 0.1	201.3 / - / 1	[10]
4	MXene/MoS_2	0.01–2	0.8M KPF6/EC+DEC	206 / 100 / 0.05	145.5 / 50 / 0.2	[11]
5	$Cu_{12}Sb_4S_{13}$ / Ti_3C_2	0.01–2.6	0.8M KPF6/EC+DEC	496.7 / 200 / 0.1	175.6 / 1800 / 1	[12]
6	MoS_2/Sb N–Doped Graphene	0.1–3.0	1M KFSI/DIG+YME	296.7 / 200 / 0.5	170.1 / 1000 / 2	[13]
7	Sb/Sb_2S_3@CHT	0.01–2.5	4M KFSI/DME	400.9 / 200 / 0.2	147.5 / 3500 / 1	[14]
8	CoS_2/Sb_2S_3@NC/CNT	0.01–3.0	0.8M KPF6/EC+DEC	453.5 / 50 / 0.2	–	[15]
9	Sb_2S_3–C@Nb_2O_5–C NFs	0.01–3.00	1M KFSI/EC+DEC	347.5 / 100 / 0.1	96.1 / 2200 / 2	[16]
10	Sb_2S_3@rGO@NC	0.01–3.0	–	211.7 / 50 / 0.05	89 / 200 / 0.2	[17]
11	V_5S_8@Cnanorod	0.01−3.0	1M KFSI/EC+DEC	468 / 100 / 0.1	171 / 4000 / 3	[18]
12	Honeycomb V_5S_8@C	0.01–3.0	–	479.1 / 500 / 0.05	121.5 / 500 / 1	[19]
13	V_5S_8@CNF	0.01–3	0.8M KPF6/EC+DEC	289.2 / 200 / 0.1	190.1 / 2000 / 1	[20]
14	VS_4/SnS@C	0.1–3.0	1M KFSI/EC+DEC	227 / 3000 / 0.5	168.4 / 6000 / 1	[21]
15	SNF-VS_2	0.5-2.5	0.75 M KPF_6/EC+DEC	389 / 100 / 0.025	98 / 500 / 0.5	[22]
16	$Ni_3Sn_2S_2$@NC	0.01-3	3M KFSI/DME	460.2 / 150 / 0.1	178.5 / 2000 / 1	[23]

Table S2. Fitting results of EIS for V_5S_8/Sb_2S_3@NC, V_5S_8@NC, and Sb_2S_3@NC electrode at fresh state and after 100th cycles.

Fresh Electrode	Rs(Ω)	Rct(Ω)	After 100th cycles	Rs(Ω)	Rct(Ω)
V_5S_8/Sb_2S_3@NC	65.43	1606	V_5S_8/Sb_2S_3@NC	52.94	1745
V_5S_8@NC	69.94	1062	V_5S_8@NC	64.96	2211
Sb_2S_3@NC	52.14	1747	Sb_2S_3@NC	32.62	3161

Fitting results of the electrochemical impedance spectroscopy (EIS) data, including the series resistance (Rs) and charge transfer resistance (Rct), were obtained for V_5S_8/Sb_2S_3@NC, V_5S_8@NC, and Sb_2S_3@NC electrodes, both in their fresh state and after 100 cycles. The equivalent circuit model contains series resistance (Rs) such as electrolyte resistance and SEI resistance, charge transfer resistance (Rct), constant phase element (CPE), and warburg resistance (Rw).

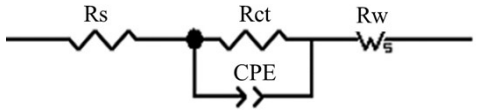

Table S3. Simulated impendence parameters (Rs and Rct) of V_5S_8/Sb_2S_3@NC electrode at different cycles.

Cycle number	Rs(Ω)	Rct(Ω)
Fresh electrode	65.43	1606
After 1st	228.5	2022
After 2nd	147.5	1785
After 5th	80.47	1664
After 50th	368.4	987.4
After 100th	52.94	1745

References:

1 G. Kresse and J. Furthmüller, Efficiency of Ab-Initio Total Energy Calculations for Metals and Semiconductors Using a Plane-Wave Basis Set, *Comput. Mater. Sci.*, 1996, **6**, 15–50.

2 G. Kresse and J. Furthmüller, Efficient Iterative Schemes for Ab Initio Total-Energy Calculations Using a Plane-Wave Basis Set, *Phys Rev B Condens Matter*, 1996, **54**, 11169–11186.

3 G. Kresse and D. Joubert, From Ultrasoft Pseudopotentials to the Projector Augmented-Wave Method, *Phys. Rev. B*, 1999, **59**, 1758–1775.

4 J. P. Perdew, J. A. Chevary, S. H. Vosko, K. A. Jackson, M. R. Pederson, D. J. Singh and C. Fiolhais, Atoms, Molecules, Solids, and Surfaces: Applications of the Generalized Gradient Approximation for Exchange and Correlation, *Phys. Rev. B*, 1992, **46**, 6671–6687.

5 J. P. Perdew, K. Burke and M. Ernzerhof, Generalized Gradient Approximation Made Simple, *Phys. Rev. Lett.*, 1996, **77**, 3865–3868.

6 H. J. Monkhorst and J. D. Pack, Special Points for Brillouin-Zone Integrations, *Phys. Rev. B*, 1976, **13**, 5188–5192.

7 V. Wang, N. Xu, J.-C. Liu, G. Tang and W.-T. Geng, VASPKIT: A User-Friendly Interface Facilitating High-Throughput Computing and Analysis Using VASP Code, *Comput. Phys. Commun.*, 2021, **267**, 108033.

8 Y. Liu, Z. Sun, X. Sun, Y. Lin, K. Tan, J. Sun, L. Liang, L. Hou and C. Yuan, Construction of Hierarchical Nanotubes Assembled from Ultrathin V_3S_4@C Nanosheets towards Alkali-Ion Batteries with Ion-Dependent Electrochemical Mechanisms, *Angew. Chem., Int. Ed.*, 2020, **59**, 2473–2482.

9 L. Xu, X. Chen, W. Guo, L. Zeng, T. Yang, P. Xiong, Q. Chen, J. Zhang, M. Wei and Q. Qian, Co-Construction of Sulfur Vacancies and Carbon Confinement in V_5S_8/CNFs to Induce an Ultra-Stable Performance for Half/Full Sodium-Ion and Potassium-Ion Batteries, *Nanoscale*, 2021, **13**, 5033–5044.

10 K. Cao, X. Su, H. Li, Y. Dong, Y. Lei and H. Liu, Surface Modification and Microstructure Regulation of SnS_2 Anodes for Improved Potassium-Ion Storage, *Appl. Surf. Sci.*, 2026, **730**, 166262.

11 J. Li, B. Rui, W. Wei, P. Nie, L. Chang, Z. Le, M. Liu, H. Wang, L. Wang and X. Zhang, Nanosheets Assembled Layered MoS_2/MXene as High Performance Anode Materials for Potassium Ion Batteries, *J. Power Sources*, 2020, **449**, 227481.

12 Y. Cao, Y. Zhang, H. Chen, S. Qin, L. Zhang, S. Guo and H. Yang, $Cu_{12}Sb_4S_{13}$ Quantum Dots/Few-Layered Ti_3C_2 Nanosheets with Enhanced K+ Diffusion Dynamics for Efficient Potassium Ion Storage, *Adv. Funct. Mater.*, 2022, **32**, 2108574.

13 L. Cao, B. Zhang, H. Xia, C. Wang, B. Luo, X. Fan, J. Zhang and X. Ou, Hierarchical Chrysanthemum-like MoS_2/Sb Heterostructure Encapsulated into N-Doped Graphene Framework for Superior Potassium-Ion Storage, *Chem. Eng. J.,* 2020, **387**, 124060.

14 Y. Wu, J. Zheng, Y. Tong, X. Liu, Y. Sun, L. Niu and H. Li, Carbon Hollow Tube-Confined Sb/Sb_2S_3 Nanorod Fragments as Highly Stable Anodes for Potassium-Ion Batteries, *ACS Appl. Mater. Interfaces*, 2021, **13**, 51066–51077.

15 X. Li, H. Liang, X. Liu, R. Sun, Z. Qin, H. Fan and Y. Zhang, Ion-Exchange Strategy of CoS_2/Sb_2S_3 Hetero-Structured Nanocrystals Encapsulated into 3D Interpenetrating Dual-Carbon Framework for High-Performance Na^+/K^+ Batteries, *Chem. Eng. J.,* 2021, **425**, 130657.

16 H. Liu, Y. He, K. Cao, S. Wang, Y. Jiang, X. Liu, K.-J. Huang, Q.-S. Jing and L. Jiao, Stimulating the Reversibility of Sb_2S_3 Anode for High-Performance Potassium-Ion Batteries, *Small*, 2021, **17**, 2008133.

17 S. Chong, S. Qiao, X. Wei, T. Li, L. Yuan, S. Dong and W. Huang, Sb_2S_3-Based Conversion-Alloying Dual Mechanism Anode for Potassium-Ion Batteries, *iScience*, 2021, **24**, 103494.

18 J. Lu, H. Tong, S. Chen, C. Wang, X. Zeng, J. Tu and Q. Chen, One-Step Construction of V_5S_8 Nanoparticles Embedded in Amorphous Carbon Nanorods for High-Capacity and Long-Life Potassium Ion Half/Full Batteries, *ACS Appl. Mater. Interfaces*, 2021, **13**, 54308–54314.
19 J. Li, S. Zhang, S. Zhang, C. An and L. Cao, Templated Constructing Honeycomb-like V_5S_8@C Anode with Multi-Scale Interfacial Coactions and High Pseudocapacitive Contribution for Enhanced Potassium Storage Capability, *J. Alloys and Compounds*, 2021, **851**, 156920.
20 S. Liu, H. Zhang, M. Zhou, X. Chen, Y. Sun and Y. Zhang, V_5S_8 Nanoparticles Anchored on Carbon Nanofibers for Fast and Durable Sodium and Potassium Ion Storage, *J. Electroanal. Chemi.*, 2021, **903**, 115841.
21 L. Cao, B. Luo, B. Xu, J. Zhang, C. Wang, Z. Xiao, S. Li, Y. Li, B. Zhang, G. Zou, H. Hou, X. Ou and X. Ji, Stabilizing Intermediate Phases via Efficient Entrapment Effects of Layered VS_4/SnS@C Heterostructure for Ultralong Lifespan Potassium-Ion Batteries, *Adv. Funct. Mater.*, 2021, **31**, 2103802.
22 J. Chen, Z. Tang, Z. Pan, W. Shi, Y. Wang, Z. Q. Tian and P. K. Shen, Template-Free Growth of Spherical Vanadium Disulfide Nanoflowers as Efficient Anodes for Sodium/Potassium Ion Batteries, *Mater. & Des.*, 2020, **192**, 108780.
23 Y. Fu, Y. Dong, J. Huo, M. Pang, H. Zhao, J. Hao and Y. Lei, Intraphase Electronic Coupling in $Ni_3Sn_2S_2$@nitrogen-Doped Carbon for High-Rate and Durable Potassium-Ion Batteries, *J. Colloid and Interface Sci.*, 2026, **712**, 140128.